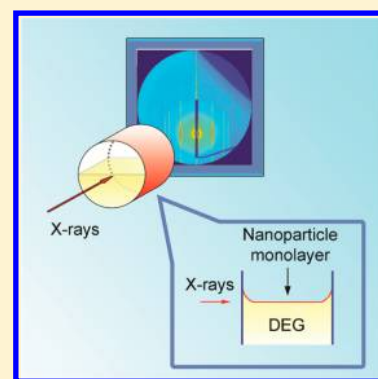


Small Angle X-ray Scattering of Iron Oxide Nanoparticle Monolayers Formed on a Liquid Surface

Datong Zhang,[†] Chenguang Lu,^{†,‡} Jiayang Hu,[†] Seung Whan Lee,^{†,§} Fan Ye,[†] and Irving P. Herman^{*,†}[†]Department of Applied Physics and Applied Mathematics, Columbia University, New York, New York 10027, United States[‡]National Center for Nanoscience and Technology, Beijing 100190, China

S Supporting Information

ABSTRACT: In situ small-angle X-ray scattering (SAXS) is used to show that iron oxide nanoparticles (NPs) of a range of sizes form hexagonally ordered monolayers (MLs) on a diethylene glycol liquid surface, after drop-casting the NPs in hexane and subsequent hexane evaporation. The formation of the ordered NP ML is followed in real time by SAXS when using a heptane solvent. During drying, the NPs remain in the hexane or heptane layer, and an ordered structure is not formed then. After drying, the NPs are farther apart than expected from only van der Waals attraction between the NP cores and Brownian motion considerations, which suggests the importance of ligand attraction in binding the NPs.



INTRODUCTION

Close packed, highly ordered two-dimensional (2D) nanoparticle (NP) layers have attracted interest in recent years because they have the properties of 2D films, including being flexible and having a large surface/volume ratio, while maintaining the zero-dimensional (0D) properties of the NPs. Ordered NP monolayers (MLs) can be formed directly on a solid surface or on a liquid surface and can be used either directly or transferred to a solid surface.^{1–5} For example, we have formed NP MLs on a liquid surface and transferred them on top of van der Waal MLs,⁵ using a liftoff technique.^{2,3} These studies point to the need to understand the NP ML formation process as an end in itself and also to help improve the transfer process and make it more versatile. Moreover, studying such NP ML films affords an opportunity to compare the formation of ordered 3D NP superlattices and 2D NP MLs. It has been seen that 2D binary or ternary superlattices form on a liquid surface much faster than the several hours needed to form 3D NP superlattices,^{2,3} which suggests that the self-assembly mechanisms for ordered 2D and 3D structures could be very different.

We used *in situ* small-angle X-ray scattering (SAXS) to study the formation of iron oxide NP MLs, formed from NPs initially dispersed in a hexane (boiling point 68 °C) or heptane (bp 98 °C) solvent that evaporates rapidly, into ordered 2D structures on the surface of the diethylene glycol (DEG) liquid. SAXS is a powerful tool that can analyze the symmetry and core–core distance of NPs in MLs.⁶ By using NPs with seven different core sizes in hexane, we were able to analyze the energetics and mechanism of 2D self-assembly of NPs and by using heptane as the solvent we were able to follow the formation of the ordered ML in real time.⁶

In our real-time SAXS investigation of the formation of 3D ordered arrays of iron oxide NPs (from drop-cast colloids in toluene/decane/dodecane mixture solvent),⁶ we showed that the larger the NP, the farther apart they are when the superlattice begins to form during solvent evaporation and the closer together they are after ordering and evaporation; this is largely due to the balance of thermal energy and the van der Waals attraction between the NP cores. The formation of ordered 2D arrays on a liquid surface could be different because the total binding energy between a NP and its nearest neighbors is smaller at the same separation. From 3D to 2D, the number of nearest neighbors decreases from 12 to 6 in hexagonal close packing, a factor of 2 (and there is partial screening by the DEG here after NP colloid solvent evaporation), while the Brownian motion energy decreases only by a factor of 1.5 (from $(3/2)k_B T$ to $k_B T$); the role of entropy can also be different.^{2,7} Ligand–ligand interactions can be important and very different in 2D and 3D assemblies.⁸ Moreover, surface tension at the liquid solvent/lower liquid or lower liquid/air interfaces is expected to be important in these 2D systems.^{9–12}

EXPERIMENTAL METHODS AND RESULTS

Figure 1a shows the cell used to assemble the monolayers and perform grazing incidence SAXS. The Teflon cell has a 7 mm path length sealed with two 2 cm diameter kapton windows, using Aflas O-rings. Because the surface between the lower

Received: February 20, 2015

Revised: April 21, 2015

Published: April 21, 2015



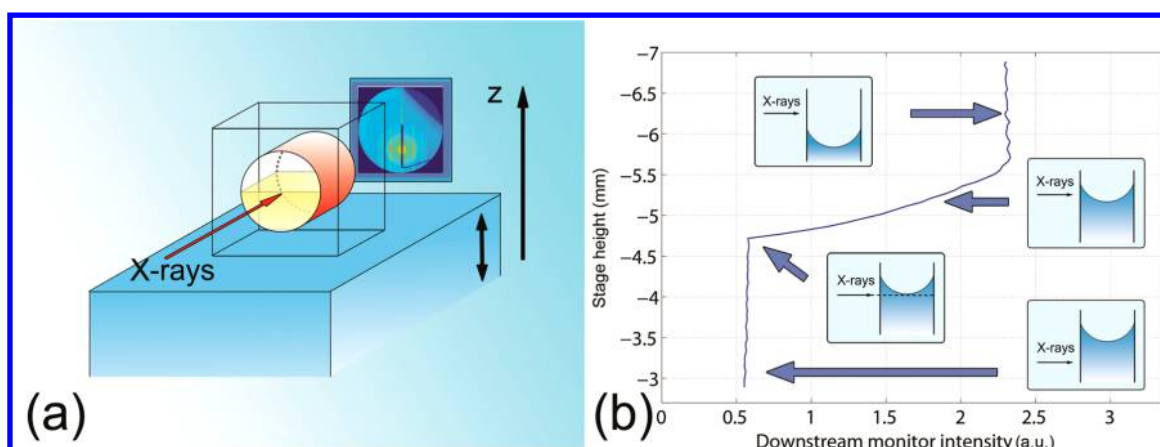


Figure 1. (a) Schematic showing the SAXS setup. (b) Alignment of the horizontal X-ray beam with the horizontal liquid surface for grazing incidence SAXS (GISAXS), by downstream monitoring of the transmitted X-ray beam as the cell is translated. Measurements are performed in the configuration of the inset with the dashed line path.

liquid (called the subphase here) and air is concave, the X-ray beam needs to pass through the liquid over much of this path (Figure 1b). There are two ~ 1 mm diameter holes on top of the cell for adding solvent and solution, and exposing the solution to the ambient environment. The cell is placed on a moving stage with precise steps as short as ~ 10 μm . In the SAXS setup we used at the Brookhaven National Laboratory (BNL) X9A beamline the X-ray beam was set to be horizontal (tilting angle = 0°), so it would be parallel to the top of the liquid surfaces (away from the meniscus, Figure 1b). The total intensity of the scattered beam can be collected by a downstream monitor after the beam passes through the sample (Figure 1b). The X-ray wavelength is 0.8793 \AA and the fwhm spot size is ~ 100 μm .

Details about preparing the 8.6 to 15.0 nm diameter iron oxide NPs,¹³ ligand treatment,¹⁴ and the use of SAXS to determine NP sizes¹⁵ (Figure S1) are presented in the Supporting Information. During each experiment 20 μL of the NP colloid (~ 0.3 mg/mL) was dropped on top of the ~ 1.4 cm^2 surface of the DEG subphase at room temperature to achieve coverage of a large fraction of monolayer coverage of NPs for all NP sizes. DEG is denser than hexane, heptane, and decane (that are used to disperse and deliver the NPs) and is immiscible with them, has a very low vapor pressure, and does not disperse the oleate-capped NPs. There is sufficient transmission of the X-rays using DEG as the subphase (the X-ray attenuation length is 7 mm at the X-ray wavelength used).¹⁶ In earlier work, we deposited NPs in hexane on top of a dimethyl sulfoxide (DMSO) subphase and then transferred the resulting NP MLs,⁵ but we did not use DMSO here because its X-ray attenuation length at the X-ray wavelength used, 1.15 mm,¹⁶ is too short to get sufficient X-ray transmission.

The cell was aligned by scanning the cell height, as shown in Figure 1b, and monitoring X-ray attenuation in the DEG with the downstream monitor. This set the X-ray trajectory relative to the liquid surface and helped in determining the geometry of the liquid surface caused by the capillary effect (schematically shown in the Figure 1b insets). During SAXS signal collection, the X-ray beam was placed 100 μm (\sim the spot diameter) above the lowest point in the liquid/air interface surface (Figure 1b, inset with the dashed line path), so measurements were in the grazing incidence regime (as corroborated by seeing linear patterns rather than elliptical patterns^{17,18}), without encounter-

ing the meniscus. The X-ray irradiation protocol is described in the Supporting Information.

All SAXS patterns taken after hexane evaporation indicate ordered ML structures with hexagonal symmetry. There is no evidence for the formation of two layers or of 3D crystallites of NPs (formed in the bulk liquid, as in ref 18). The pattern of the ML formed by 11.8 ± 0.8 nm NPs is shown in Figure 2. SAXS

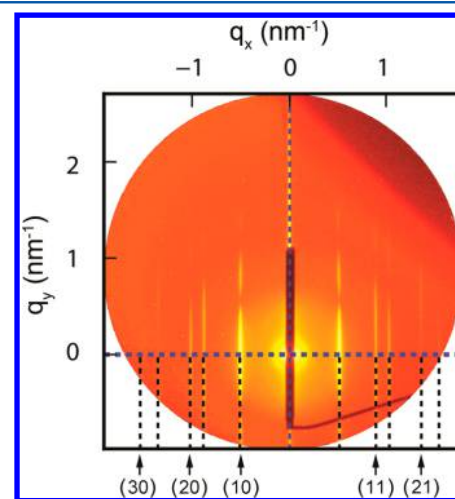


Figure 2. In situ SAXS pattern of a ML of 11.8 nm diameter NPs. The separation of cores is fit by the first five peaks: (1 0), (1 1), (2 0), (2 1), and (3 0).

patterns looked the same each measurement cycle for each NP/hexane run (which meant that the ML was in the final ordered state each time). Aside from different scaling, the SAXS patterns were similar for different NP sizes. The SAXS pattern in Figure 2 indicates an ordered NP ML formed after hexane evaporation. NP core–core distances were extracted from these patterns by fitting the peak position for the (1 0), (1 1), (2 0), (2 1), and (3 0) diffraction orders. Figure 3 shows the final separations of the surfaces of the cores of nearest-neighbor NPs in MLs for different NP core diameters for each hexane run, which were determined by subtracting the diameter obtained (see the Supporting Information) from the separation of the centers of the NPs obtained from the SAXS pattern. (This includes all measurements made using hexane during the first visit to BNL, which included two runs for each particle size, and

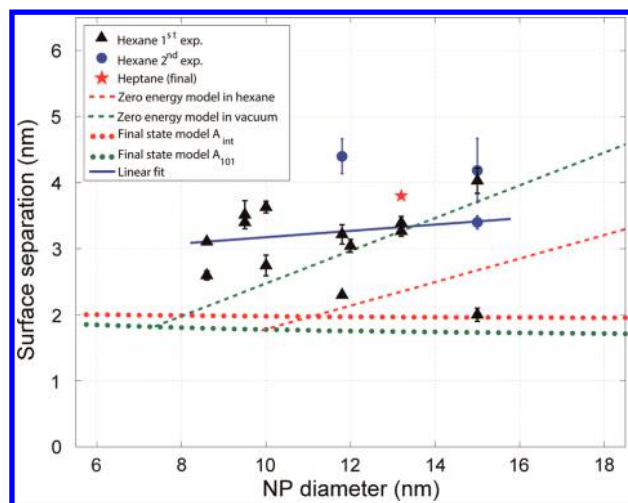


Figure 3. Separation of the core surfaces of nearest-neighbor iron oxide NPs, as measured by *in situ* SAXS after hexane and heptane drying, vs NP diameter. A linear fit to these points is shown, along with model predictions showing the separation when the core–core van der Waals attraction energies (in vacuum and hexane) equals the thermal energy and the energy at the final separation, assuming these two energies and ligand repulsion, which is bounded by the final energy plots assuming two different limits, with no screening by DEG, so $A_{int} = A_{101}$ (labeled as A_{101}), and with complete screening by DEG, so $A_{int} = 8.0$ zJ (labeled as A_{int}). The error bars represent the least-squares error of the several measurement cycles during a given run.

the second visit, when the measurements were repeated for the 11.8 and 15.0 nm NPs because the measurements at each of these two sizes gave very different results during the first visit (Figure 3). All runs for a given size of NPs were conducted with the same batch of NPs.) The error bars are the standard deviations of the multiple SAXS images obtained during each self-assembly run. (Variations in X-ray alignment is a potential cause of the random run-to-run scatter in the measured NP separations for a given NP size. Other potential causes include the statistical nature of nucleation and growth during assembly,¹⁹ slight variations in the ambient environment, and variations in ligand coverage due to the statistical nature of the synthesis and washing procedures and of NP aging.)

The formation of clustered regions of NP MLs was confirmed by monitoring the surface in real time using optical microscopy in parallel experiments where 10.0 nm NPs in hexane were drop-cast on DEG in a Petri dish (see the Supporting Information). Under conditions similar to those examined with SAXS, an apparently continuous monolayer of NPs formed in a ring-like pattern as the hexane dried; this ring filled in (totally or partially) as the remaining hexane colloid in the central region continued to evaporate, with NPs added to the shrinking inner ring. When many fewer NPs were drop-cast (than in these and the SAXS experiments), the NPs still clustered together when the hexane evaporated to form a ML (which still appeared to be continuous, given the limited resolution of optical microscopy), though the fraction of the overall surface covered by this ML was smaller. When many more NPs were drop-cast, a double layer formed in the center and a multilayer ridge formed in the outer periphery (similar to the commonly seen “coffee rings”²⁰ seen in after NP colloids are drop-cast and allowed to dry on solid surfaces^{21–24}).

Figure 4 shows a representative series of SAXS patterns of 13.2 nm NPs obtained as the heptane solvent dried.

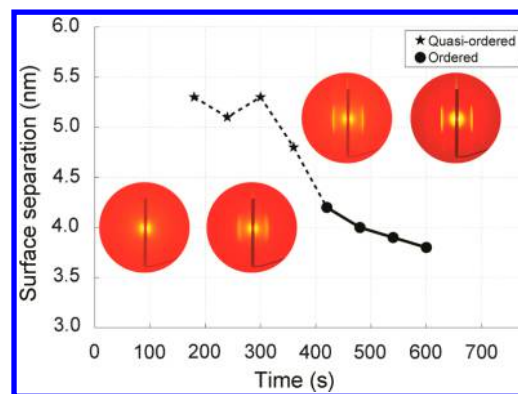


Figure 4. SAXS images and the separations of the core surfaces of nearest-neighbor iron oxide NPs during the formation of a hexagonally ordered array, along with representative SAXS images, after drop-casting 13.2 nm NPs in heptane. The formation of quasi-ordered MLs begins at ~ 180 s, followed by fully ordered ML starting at ~ 420 s.

Measurements were made every minute for 10 s, starting at 2 min after drop-casting. No pattern was seen at 2 min, which means that the NPs were initially dispersed in the heptane layer (and there were no 2D MLs at the heptane/DEG or heptane/air interfaces). Then only the (1 0) feature was seen from 3 to 6 min, as the particles became closer. At 7 min, the (1 0) feature became sharp and other orders appeared, indicating an ordered structure, as the separation decreased from ~ 4.2 nm to ~ 3.8 nm. This final point (after the heptane had fully evaporated) is also plotted in Figure 3. (Better time resolution is possible.²⁵ Sequential measurements shorter than 10 s were possible here, but were not needed due to the observed evaporation rate of heptane. With hexane, the limiting factor for real-time measurements was the setup time and not the time resolution of the SAXS measurements.) No pattern was seen with decane (bp 174 °C) as the NP solvent, because it did not totally evaporate during the irradiation cycle, and 2D NP films did not form at either interface.

The separation of nearest-neighbor NPs after drying changes from ~ 3.1 nm for 8.6 nm NPs to ~ 3.5 nm for 15 nm NPs, as seen in the linear fit in Figure 3. This suggests perhaps a weak increase NP size (within the scatter of the data). The separation of the 13.2 nm NPs after heptane evaporation is consistent with that for runs with the same NPs in hexane. All of these final core–core separations were much larger (by ~ 2 nm) than that observed in dried 3D lattices of the same particles, which decreased from ~ 1.5 nm to ~ 1.0 nm for particle sizes from 10 to 15 nm.⁶

DISCUSSION

The assembly process is modeled by first evaluating the energies and locations of individual NPs during the drying of the alkane solvent and then the energies of individual NPs and of the NP assembly at the DEG/air interface after drying.

A simple model of the interfacial energy of individual noninteracting spherical NPs at fluid/fluid interfaces is used to track them during drying, when they might be energetically favored to be at the alkane/air interface, in the alkane layer, and/or at the DEG/alkane interface, and then to analyze the NP ML after drying, when they are at the DEG/air interface. In equilibrium, the NP energy at the interface of fluids 1 and 2 are estimated by using Pieranski’s model²⁶

$$\Delta E = -\pi R^2 \gamma_{1/2} \left(1 - \frac{\gamma_{p/2} - \gamma_{p/1}}{\gamma_{1/2}} \right)^2$$

with $\frac{\gamma_{p/2} - \gamma_{p/1}}{\gamma_{1/2}} < 1$ (1)

relative to the energy of the NPs in the bulk of the fluid with the lower surface tension (fluid 1 here), where R is the particle radius, $\gamma_{a/b}$ is the surface tension for interface a and b , with 1 and 2 standing for the two fluids and p for the particles. If $((\gamma_{p/2} - \gamma_{p/1})/(\gamma_{1/2})) \geq 1$ at the interface, binding is not expected in this model.

The surface properties of NPs are assumed to be dominated by the surface ligands, here the oleate (and there is no exposed core surface). The surface tension for a liquid in air is used: $\gamma_{\text{hex}} = 18.4$ mN/m for hexane (and 20.14 mN/m for heptane),^{27,28} $\gamma_{\text{DEG}} = 44.77$ mN/m for DEG,²⁸ and $\gamma_{\text{OA}} = 32.79$ mN/m for oleic acid²⁹ (OA) (for the NP surface tension), and $\gamma_{\text{DEG/hexane}} = 9.9$ mN/m for the DEG/hexane interface (and 10.6 mN/m for DEG/heptane).^{30,31} Absent experimental measurement, the OA/DEG and OA/alkane interfacial surface tensions are characterized by using^{32,33}

$$\gamma_{1/2} = \gamma_1 + \gamma_2 - 2\Phi_{1/2} \sqrt{\gamma_1 \gamma_2} \quad (2)$$

where γ_1 and γ_2 are the surface tensions of the liquid with air and $\Phi_{1/2}$ is a dimensionless quantity that usually ranges from 0.5 to 1.15.³³ Φ is larger for similar solvents, with smaller interfacial tension.

Figure 5b is a minimum energy “phase” diagram showing the medium in which the NPs are expected to have the lowest energy in equilibrium, with $\Phi_{\text{OA/DEG}}$ and $\Phi_{\text{OA/hexane}}$ as parameters. $\gamma_{\text{OA/DEG}}$ is estimated to be the same as that for the octadecane/DEG interface, 12.8 mN/m,³⁰ because the single C–C double bond in OA should have little effect on surface tension (as is true for two molecules for which data are available that also differ in that one has a single carbon–carbon bond replaced by a double bond: C_5H_{10} (15.45 mN/m) and C_5H_{12} (15.49 mN/m)²⁸), and so $\Phi_{\text{OA/DEG}}$ should be ~ 0.84 . Then the NPs would be in the bulk hexane as it evaporates for $\Phi_{\text{OA/hexane}} > 0.99$ (0.99 also for OA/heptane). Because OA and hexane are miscible, the surface tension should be negative or close to zero,³⁴ so eq 2 shows that $\Phi_{\text{OA/hexane}}$ should be ~ 1.04 or larger (~ 1.03 or larger for OA/heptane). For $\Phi_{\text{OA/DEG}} = 0.84$ and $\Phi_{\text{OA/hexane}} = 1.04$, the NPs have lowest energy in the bulk, evaporating hexane layer, though this point (closed circle in Figure 5b) is near the boundary with the hexane/DEG interface (and this is also true for the free energy because the entropy is higher in the bulk liquid); the same conclusions are also valid with the heptane solvent. The energy of the individual 10 nm diameter NPs in each medium is plotted in Figure 5a for these parameters (solid line); they are bound to the hexane layer by about a thousand $k_B T_{\text{room}}$ for NPs of this size. This is also plotted for $\Phi_{\text{OA/DEG}} = 0.95$; if this had been the parameter, the NPs would have been energetically most stable at the DEG/hexane interface (dashed line, with the open circle marking the NP location in Figure 5a and the point of minimum energy in Figure 5b).

This suggests that the NPs are expected to largely remain in the evaporating alkane layer and do not assemble there. This is confirmed in the time-resolved study with the heptane solvent, which showed that the ordered 2D NP layer does not initially form at either interface, but gradually forms near the heptane/

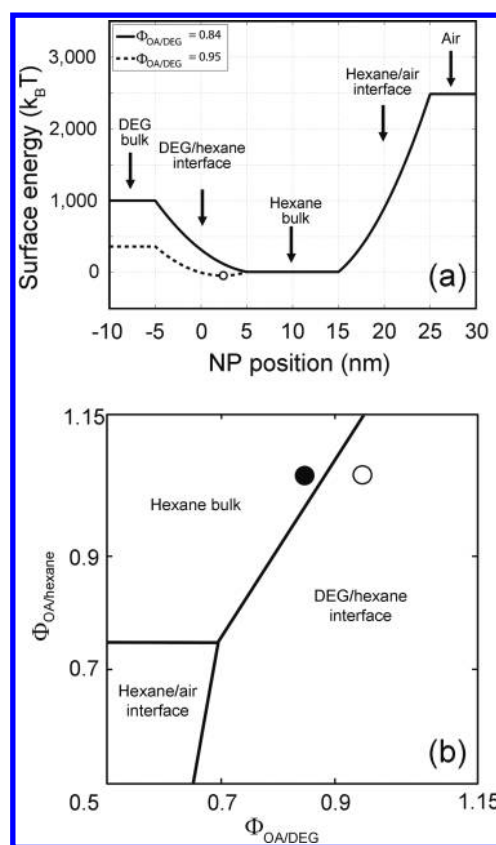


Figure 5. (a) Energy of 10 nm oleate-capped iron oxide NPs due to surface tension, plotted across from the bulk DEG/DEG–hexane interface/bulk hexane (whose width is drawn much smaller than scale)/hexane–air interface/air. The solid line is based on the expected values of $\Phi_{\text{OA/DEG}} = 0.84$ and $\Phi_{\text{OA/hexane}} = 1.04$ and shows the minimum energy is in bulk hexane; the dashed line shows the minimum energy would be at the DEG/hexane interface (at the open circle) for the hypothetical case with $\Phi_{\text{OA/DEG}} = 0.95$ and $\Phi_{\text{OA/hexane}} = 1.04$. (b) Minimum energy “phase” diagram showing the medium where these NPs dispersed in hexane and drop-cast on DEG would have minimum energy, as a function of $\Phi_{\text{OA/DEG}}$ and $\Phi_{\text{OA/hexane}}$; this is independent of particle size. The solid circle, at the expected values of $\Phi_{\text{OA/DEG}} = 0.84$ and $\Phi_{\text{OA/hexane}} = 1.04$, shows the NPs have lowest energy in the bulk, evaporating hexane layer. The hypothetical example in (a) with $\Phi_{\text{OA/DEG}} = 0.95$, is plotted as an open circle (corresponding to the open circle in part a).

DEG interface, which becomes the DEG/air interface after heptane evaporation. The supporting optical microscopy experiments suggest that solvent evaporation and the deposition of the NPs at the DEG/air interface do not occur simultaneously across the surface; as the alkane in the central region of the NP colloid drop evaporates and the central region becomes smaller, the NPs at the edge of the remaining hexane droplet are left at the DEG/air interface and the continuous NP ML region grows.

After hexane evaporation, the NPs are at the DEG/air surface (and do not disperse in the DEG). Using Pieranski’s model, the center of an NP with radius R is $Z = 0.45R$ below this interface. Therefore, during the final stages of drying, which occurs locally at the edge of the evaporating hexane droplet, the NPs move from the alkane layer partially into the DEG, pushed by surface tension from the upper surface of the hexane layer. These vertical forces are accompanied by a deformation of the liquid surface that creates lateral attraction forces, which are ~ 3 orders

of magnitude larger than $k_B T_{room}$ for 10 nm diameter NPs.^{11,35,36} Such motion has been confirmed by computer simulations that show that such forces can produce ordered 2D NP MLs.¹¹ The NPs are seen to be bound to the DEG/air interface by $\sim 260k_B T_{room}$ relative to the bulk DEG for 10 nm NPs; for smaller coverages, this strong binding promotes 2D rather than 3D NP assembly.

The NP separation after solvent evaporation is determined by modifying the model of the energy of 3D NP arrays^{6,37} to 2D; the Brownian motion energy is smaller by a factor of 1.5 and other interaction energies (vdW attraction and ligand repulsion at smaller separations) are smaller by a factor of 2, because the nearest-neighbor number decreases from 12 to 6. In this 2D model, the energy is relative to the interfacial energy of individual NPs. The vdW energy for each pair of nearest-neighbor interactions, is

$$E_{vdW} = -\frac{A}{6} \left[\frac{2R^2}{h^2 + 4Rh} + \frac{2R^2}{h^2 + 4Rh + 4R^2} + \ln \left(\frac{h^2 + 4Rh}{h^2 + 4Rh + 4R^2} \right) \right] \quad (3)$$

where A is the Hamaker constant, R is the NP radius, and h is the separation of the core surfaces. This separation is plotted in Figure 3 when the total energy due to van der Waals core–core attraction and Brownian motion is zero for NPs in vacuum ($A_{101} = 43$ zJ) (isolated NP ML cores) and in hexane ($A_{131} = 22$ zJ) (potential screening by hexane during drying), without ligand–ligand interactions.³⁸ In 2D, the NPs need to be closer than in 3D for the vdW attraction to balance Brownian motion. The separation is also shown for minimum energy, when the NPs are closer and only for cases with negative energy; this includes thermal energy, core–core van der Waals attraction (which is partially screened by DEG and ligands in the final state), osmotic pressure, and ligand repulsion, as in ref 37. The Hamaker constant for the NP core at the DEG/air interface is estimated using the model from ref 39, with $A_{int} = A_{101} + f^2(3 - 2f)(A_{13'1} - A_{101})$, where $f = (Z + R)/2R = 0.725$ is the linear fractional immersion and A_{int} , $A_{13'1}$, and A_{101} are the Hamaker constants of the interface, liquid (DEG here) and air, respectively. Because $A_{13'1}$ is not known, this final energy is plotted in Figure 3 assuming two extreme limits $A_{13'1} = A_{101}$ (no screening by DEG, so $A_{int} = A_{101}$) and $A_{13'1} = 0$ zJ (complete screening by DEG, so $A_{int} = 8.0$ zJ).

The model final state separation decreases very weakly with increasing NP size in contrast to the observed very weak increase. Likely more significant than these weak variations with NP size is the conclusion that these model final state separations are at least 1 nm smaller than those measured. Moreover, the thermal energies of the NPs exceed the core–core van der Waals attraction energy at the measured separations, so the array can be bound only if there are other attractive forces, which must be due to attraction between the ligands on neighboring NPs. The NP separations are a little smaller than twice the fully extended length of the oleate ligands of ~ 2.2 nm, so even with ligand attraction there appears to be little ligand interdigitation or compression. (After hexane evaporation, NP–NP binding due to surface tension at equilibrium is negligible, because the effect of gravity on the NPs is too small to create significant curvature of the liquid DEG surface.^{35,36}) Density functional theory shows that the interaction energy between C–C dimers in adjacent ligands is

~ 0.8 kcal/mol, which is $\sim 1.4k_B T_{room}$.⁴⁰ The oleate ligands would be expected to be retracted because of their high surface tension in interfaces with DEG and air. An estimate of the number of interactions provides a very rough estimate of the net ligand–ligand attraction per NP on the order of a hundred $k_B T_{room}$, so the energy that binds the NPs to each other (which needs to be at least several $k_B T_{room}$ per NP to have the observed ML stability) may be weaker than the energy that binds them to the DEG/air interface.

Assembly might also be influenced by the entropic contribution to the free energy. The ordered state of noninteracting hard disks has higher entropy than the disordered state above $\sim 79.8\%$ of the close-packed concentration,⁴¹ so the observed ordered states of NPs, likely bound mostly by ligand–ligand attraction, have lower free energy due to entropy than would disordered states. However, entropy does not favor the assembly of hard disks; the entropy (of the highest entropy state) decreases as the disks get closer. Close-packed assemblies are always seen here by TEM, for NP coverages of $\sim 5\%$ – 50% of the closed pack concentration averaged over the entire surface, which also suggests that the total NP–NP attraction energy and not entropy is the dominant term in the free energy. In any case, entropy appears to make a small contribution, $< k_B$ entropy per NP ($< k_B T_{room}$ free energy per NP).⁴¹

CONCLUSIONS

In situ small-angle X-ray scattering was used to probe the formation of iron oxide NP MLs after drop-casting colloids of NPs in alkanes on a DEG subphase. Hexagonally ordered arrays formed when using NPs dispersed in hexane, which were probed after solvent evaporation for a range of NP sizes, and in heptane, which were probed during solvent evaporation. During drying, SAXS shows that NPs were in the hexane or heptane layer, and not at the alkane interfaces with air or DEG, and this was confirmed by modeling the surface energy of the NPs. The ordered monolayer formed at the final stages of drying or perhaps later. Real-time optical microscopy suggests the formation of a monolayer, and one that is formed at the outer edges of the colloid drop where it meets the DEG/air/NP ML interface. After drying, the NPs in these 2D arrays on DEG were ~ 2 nm farther apart than that measured in fully dried 3D arrays. The NPs in the ML were roughly ~ 1 nm farther apart than expected from a model that included only van der Waals attraction and Brownian motion considerations (which successfully modeled the separations in 3D arrays in previous studies), which suggests the importance of ligand–ligand stabilization in binding the NPs to each other in these 2D arrays assembled on a liquid; ligand–ligand attraction likely also stabilizes NP ordering. These findings can help guide the rational design and subsequent use of ordered NP monolayers, including designing the NP separation and perhaps symmetry.

ASSOCIATED CONTENT

Supporting Information

NP preparation and ligand treatment, SAXS determination of NP sizes, the X-ray irradiation protocol, and optical microscopy monitoring. The Supporting Information is available free of charge on the ACS Publications website at DOI: 10.1021/acs.jpcc.5b01741.

■ AUTHOR INFORMATION

Corresponding Author

*(I.P.H.) E-mail: iph1@columbia.edu.

Present Address

§National Fusion Research Institute in Korea, Daejeon, South Korea

Notes

The authors declare no competing financial interest.

■ ACKNOWLEDGMENTS

Support was provided by the MIRT program of the National Science Foundation (DMR-1122594), the NSF MRSEC program through Columbia in the Center for Precision Assembly of Superstratic and Superatomic Solids (DMR-1420634), and the EFRC program of DoE (DE-SC0001085), by the New York State Office of Science, Technology, and Academic Research, and a gift by the Honda Research Institute. Use of the National Synchrotron Light Source (NSLS), Brookhaven National Laboratory, was supported by the U.S. Department of Energy, Office of Science, Office of Basic Energy Sciences, under contract number DE-AC02-98CH10886. We thank Drs. Lin Yang and Masafumi Fukuto for their assistance at the NSLS X9A beamline, Prof. Sanat Kumar for very helpful discussions, and Kathleen Kennedy for assistance in some experiments.

■ REFERENCES

- (1) Aleksandrovic, V.; Greshnykh, D.; Randjelovic, I.; Froemdsdorf, A.; Kornowski, A.; Roth, S. V.; Klinke, C.; Weller, H. Preparation and Electrical Properties of Cobalt-Platinum Nanoparticle Monolayers Deposited by the Langmuir-Blodgett Technique. *ACS Nano* **2008**, *2*, 1123–1130.
- (2) Dong, A.; Ye, X.; Chen, J.; Murray, C. B. Two-Dimensional Binary and Ternary Nanocrystal Superlattices: The Case of Monolayers and Bilayers. *Nano Lett.* **2011**, *11*, 1804–1809.
- (3) Dong, A.; Chen, J.; Vora, P. M.; Kikkawa, J. M.; Murray, C. B. Binary Nanocrystal Superlattice Membranes Self-Assembled at the Liquid-Air Interface. *Nature* **2010**, *466*, 474–477.
- (4) Bigioni, T. P.; Lin, X. M.; Nguyen, T. T.; Corwin, E. I.; Witten, T. A.; Jaeger, H. M. Kinetically Driven Self Assembly of Highly Ordered Nanoparticle Monolayers. *Nat. Mater.* **2006**, *5*, 265–270.
- (5) Lu, C.; Zhang, D.; van der Zande, A.; Herman, I. P. Electronic Transport in Nanoparticle Monolayers Sandwiched between Graphene Electrodes. *Nanoscale* **2014**, *6*, 14158–14162.
- (6) Lu, C.; Akey, A. J.; Dahlan, C. J.; Zhang, D.; Herman, I. P. Resolving the Growth of 3D Colloidal Nanoparticle Superlattices by Real-Time Small-Angle X-ray Scattering. *J. Am. Chem. Soc.* **2012**, *134*, 18732–18738.
- (7) Chen, Z.; O'Brien, S. Structure Direction of II-VI Semiconductor Quantum Dot Binary Nanoparticle Superlattices by Tuning Radius Ratio. *ACS Nano* **2008**, *2*, 1219–1229.
- (8) Mueggenburg, K. E.; Lin, X.; Goldsmith, R. H.; Jaeger, H. M. Elastic Membranes of Close-Packed Nanoparticle Arrays. *Nature Mater.* **2007**, *6*, 656–660.
- (9) Lin, Y.; Boker, A.; Skaff, H.; Cookson, D.; Dinsmore, A. D.; Emrick, T.; Russell, T. P. Nanoparticle Assembly at Fluid Interfaces: Structure and Dynamics. *Langmuir* **2005**, *21*, 191–194.
- (10) Kutuzov, S.; He, J.; Tangirala, R.; Emrick, T.; Russell, T. P.; Böker, A. On the Kinetics of Nanoparticle Self-Assembly at Liquid/liquid Interfaces. *Phys. Chem. Chem. Phys.* **2007**, *9*, 6351–6358.
- (11) Fujita, M.; Nishikawa, H.; Okubo, T.; Yamaguchi, Y. Multiscale Simulation of Two-Dimensional Self-Organization of Nanoparticles in Liquid Film. *Jpn. J. Appl. Phys. Part 1* **2004**, *43*, 4434–4442.
- (12) Garbin, V.; Crocker, J. C.; Stebe, K. J. Nanoparticles at Fluid Interfaces: Exploiting Capping Ligands to Control Adsorption, Stability and Dynamics. *J. Colloid Interface Sci.* **2012**, *387*, 1–11.
- (13) Hyeon, T.; Lee, S. S.; Park, J.; Chung, Y.; Na, H. B. Synthesis of Highly Crystalline and Monodisperse Maghemite Nanocrystallites without a Size-Selection Process. *J. Am. Chem. Soc.* **2001**, *123*, 12798–12801.
- (14) Ji, X.; Copenhaver, D.; Sichmeller, C.; Peng, X. Ligand Bonding and Dynamics on Colloidal Nanocrystals at Room Temperature: The Case of Alkylamines on CdSe Nanocrystals. *J. Am. Chem. Soc.* **2008**, *130*, 5726–5735.
- (15) Rieker, T.; Hanprasopwattana, A.; Datye, A.; Hubbard, P. Particle Size Distribution Inferred From Small-Angle X-ray Scattering and Transmission Electron Microscopy. *Langmuir* **1999**, *15*, 638–641.
- (16) Lawrence Berkeley National Laboratory Data Base.
- (17) Jiang, Z.; Lin, X.; Sprung, M.; Narayanan, S.; Wang, J. Capturing the Crystalline Phase of Two-Dimensional Nanocrystal Superlattices in Action. *Nano Lett.* **2010**, *10*, 799–803.
- (18) Narayanan, S.; Wang, J.; Lin, X. Dynamical Self-Assembly of Nanocrystal Superlattices During Colloidal Droplet Evaporation by in situ Small Angle X-ray Scattering. *Phys. Rev. Lett.* **2004**, *93*, 135503.
- (19) Roth, S. V.; Muller-Buschbaum, P.; Timmann, A.; Perlich, J.; Gehrke, R. Structural Changes in Gradient Colloidal Thin Gold Films Deposited from Aqueous Solution. *J. Appl. Crystallogr.* **2007**, *40*, s346–s349.
- (20) Yunker, P. J.; Still, T.; Lohr, M. A.; Yodh, A. G. Suppression of the Coffee-Ring Effect by Shape-Dependent Capillary Interactions. *Nature* **2011**, *476*, 308–311.
- (21) Deegan, R. D.; Bakajin, O.; Dupont, T. F.; Huber, G.; Nagel, S. R.; Witten, T. A. Capillary Flow as the Cause of Ring Stains from Dried Liquid Drops. *Nature* **1997**, *389*, 827–829.
- (22) Denkov, N. D.; Velev, O. D.; Kralchevsky, P. A.; Ivanov, I. B.; Yoshimura, H.; Nagayama, K. Two-Dimensional Crystallization. *Nature* **1993**, *361*, 26.
- (23) Roth, S. V.; Autenrieth, T.; Grübel, G.; Riekel, C.; Burghammer, M.; Hengstler, R.; Schulz, L.; Müller-Buschbaum, P. In situ Observation of Nanoparticle Ordering at the Air-Water-Substrate Boundary in Colloidal Solutions using X-ray Nanobeams. *Appl. Phys. Lett.* **2007**, *91*, 091915.
- (24) Majkova, E.; Siffalovic, P.; Chitu, L.; Jergel, M.; Luby, S.; Timmann, A.; Roth, S. V.; Satka, A.; Keckes, J.; Maier, G. A. Real-Time Tracking of Nanoparticle Self-Assembling Using GISAXS. *Superlattices Microstruct.* **2009**, *46*, 286–290.
- (25) Siffalovic, P.; Majkova, E.; Chitu, L.; Jergel, M.; Luby, S.; Capek, I.; Satka, A.; Timmann, A.; Roth, S. V. Real-Time Tracking of Superparamagnetic Nanoparticle Self-Assembly. *Small* **2008**, *4*, 2222–2228.
- (26) Pieranski, P. Two-Dimensional Interfacial Colloidal Crystals. *Phys. Rev. Lett.* **1980**, *45*, 569–572.
- (27) Birdi, K. S. *Handbook of Surface and Colloid Chemistry*; CRC Press: Boca Raton, FL, 1997.
- (28) *CRC Handbook*, 95th ed.; CRC Press: Boca Raton, FL, 2014.
- (29) Chumpitaz, L. D. A.; Coutinho, L. F.; Meirelles, A. J. A. Surface Tension of Fatty Acids and Triglycerides. *J. Am. Oil Chem. Soc.* **1999**, *76*, 379–382.
- (30) Gaines, G. L.; Gaines, G. L. Interfacial-Tension between Normal-Alkanes and Poly(ethylene glycols). *J. Colloid Interface Sci.* **1978**, *63*, 394–398.
- (31) Leibnitz, E.; Könnicke, H. G.; Niese, S. Über Ternäre Flüssige Systeme. IV. *J. Prakt. Chem.* **1957**, *4*, 286–297.
- (32) Girifalco, L. A.; Good, R. J. A Theory for the Estimation of Surface and Interfacial Energies. 1. Derivation and Application to Interfacial Tension. *J. Phys. Chem.* **1957**, *61*, 904–909.
- (33) Good, R. J.; Elbing, E. Generalization of Theory for Estimation of Interfacial Energies. *Ind. Eng. Chem.* **1970**, *62*, 54–78.
- (34) Vanoss, C. J.; Ju, L.; Chaudhury, M. K.; Good, R. J. Estimation of the Polar Parameters of the Surface-Tension of Liquids by Contact-Angle Measurements on Gels. *J. Colloid Interface Sci.* **1989**, *128*, 313–319.

- (35) Kralchevsky, P. A.; Nagayama, K. Capillary Interactions between Particles Bound to Interfaces, Liquid Films and Biomembranes. *Adv. Colloid Interface Sci.* **2000**, *85*, 145–192.
- (36) Kralchevsky, P. A.; Denkov, N. D. Capillary Forces and Structuring in Layers of Colloid Particles. *Curr. Opin. Colloid Interface Sci.* **2001**, *6*, 383–401.
- (37) Saunders, S. R.; Eden, M. R.; Roberts, C. B. Modeling the Precipitation of Polydisperse Nanoparticles Using a Total Interaction Energy Model. *J. Phys. Chem. C* **2011**, *115*, 4603–4610.
- (38) Faure, B.; Salazar-Alvarez, G.; Bergstrom, L. Hamaker Constants of Iron Oxide Nanoparticles. *Langmuir* **2011**, *27*, 8659–8664.
- (39) Williams, D. F.; Berg, J. C. The Aggregation of Colloidal Particles at the Air-Water-Interface. *J. Colloid Interface Sci.* **1992**, *152*, 218–229.
- (40) Goursot, A.; Mineva, T.; Kevorkyants, R.; Talbi, D. Interaction between n-alkane Chains: Applicability of the Empirically Corrected Density Functional Theory for Van der Waals Complexes. *J. Chem. Theory Comput.* **2007**, *3*, 755–763.
- (41) Hoover, W. G.; Ree, F. H. Melting Transition and Communal Entropy for Hard Spheres. *J. Chem. Phys.* **1968**, *49*, 3609–3617.